

Interplay between Ferroelastic and Metal–Insulator Phase Transitions in Strained Quasi-Two-Dimensional VO₂ Nanoplatelets

Alexander Tselev,^{*,†} Evgheni Strelcov,[‡] Igor A. Luk'yanchuk,[§] John D. Budai,^{||} Jonathan Z. Tischler,^{||} Iliia N. Ivanov,[†] Keith Jones,[⊥] Roger Proksch,[⊥] Sergei V. Kalinin,[†] and Andrei Kolmakov^{*,†}

[†]The Center for Nanophase Materials Sciences, Oak Ridge National Laboratory, Oak Ridge, Tennessee 37831,

[‡]Physics Department, Southern Illinois University Carbondale, Carbondale, Illinois 62901, [§]Laboratory of

Condensed Matter Physics, University of Picardie Jules Verne, Amiens, 80039, France, and L. D. Landau Institute for Theoretical Physics, Moscow, Russia, ^{||}Materials Science & Technology Division, Oak Ridge National Laboratory, Oak Ridge, Tennessee 37831, and [⊥]Asylum Research, Santa Barbara, California 93117

ABSTRACT Formation of ferroelastic twin domains in vanadium dioxide (VO₂) nanosystems can strongly affect local strain distributions, and hence couple to the strain-controlled metal–insulator transition. Here we report polarized-light optical and scanning microwave microscopy studies of interrelated ferroelastic and metal–insulator transitions in single-crystalline VO₂ quasi-two-dimensional (quasi-2D) nanoplatelets (NPIs). In contrast to quasi-1D single-crystalline nanobeams, the 2D geometric frustration results in emergence of several possible families of ferroelastic domains in NPIs, thus allowing systematic studies of strain-controlled transitions in the presence of geometrical frustration. We demonstrate the possibility of controlling the ferroelastic domain population by the strength of the NPI-substrate interaction, mechanical stress, and by the NPI lateral size. Ferroelastic domain species and domain walls are identified based on standard group-theoretical considerations. Using variable temperature microscopy, we imaged the development of domains of metallic and semiconducting phases during the metal–insulator phase transition and nontrivial strain-driven reentrant domain formation. A long-range reconstruction of ferroelastic structures accommodating metal–insulator domain formation has been observed. These studies illustrate that a complete picture of the phase transitions in single-crystalline and disordered VO₂ structures can be drawn only if both ferroelastic and metal–insulator strain effects are taken into consideration and understood.

KEYWORDS Vanadium dioxide, metal–insulator phase transition, ferroelastic phase transition, domain structure, near-field microwave microscopy

VO₂ is a strongly correlated electron material, which undergoes a first-order metal–insulator phase transition (MIT) with a few orders of magnitude change of conductivity and associated structural transition at a temperature of about 68 °C in the unconstrained bulk. The lattice structure of the high-temperature metallic phase is tetragonal (R, rutile), and the low-temperature semiconducting phase is monoclinic (M1). The transition is accompanied by a fast ($\sim 10^{-13}$ s) change in the dielectric function, which has sparked numerous potential applications of VO₂ in ultrafast modulators, switchable polarizers, beam-steering, and thermochromic devices operable from submillimeter up to near-IR range.^{1,2} It has been shown that the MIT can be induced by an electric field in two- or three-terminal devices^{3,4} as well as by light^{5,6} and that the transition temperature can be altered significantly via appropriate doping and/or uniaxial mechanical stress.⁷ Due to the responsiveness of key electronic and optical properties of VO₂ to a variety of the

aforementioned external stimuli, VO₂ has become a classical example of a so-called smart material.⁸

Recently, much attention has been attracted to the applications of nanocrystalline VO₂ in the form of thin films and nanoscale crystals.^{9–19} Nanoscale VO₂ single crystals can sustain strains without fracture and can be almost defect-free, potentially enabling fabrication of nano- and mesoscopic devices with superior characteristics. In addition, the lack of frozen disorder and exclusion of long-range strain fields make nanoscale VO₂ an ideal model system for deeper understanding of the MIT itself,¹⁸ the physics of which is still not fully understood despite half a century of research since the discovery of the phenomenon.^{12,17,20} Most reports have dealt with quasi-one-dimensional (quasi-1D) nano- and mesostructures. In particular, formation of longitudinal heterophase-metal/semiconductor-domain structures in VO₂ nanobeams and their response to elastic stress near the transition temperature were under investigation in refs 15, 18, and 19. Self-ordering of heterophase domains along the nanobeam length in the presence of elastic interactions with a substrate has been described in refs

* Corresponding authors, akolmakov@physics.siu.edu and tseleva@ornl.gov.

Received for review: 11/16/2009

Published on Web: 05/10/2010



15 and 19. In refs 18, 19, 21, and 22, it was demonstrated that in quasi-1D nanobeams, the longitudinal metal/insulator domain structure is highly sensitive to bending and uniaxial stress, and it is possible to actively control the phase inhomogeneity and the MIT temperature via stress manipulation.¹⁹

However, an important and almost completely unexplored aspect of this material is the ferroelasticity of the low-temperature monoclinic VO₂ phase with possible nontrivial coupling between the ferroelastic domain structure and strain-controlled metal–insulator transition in this oxide. Ferroelastic twinning provides a pathway to minimization of strain energy that competes with the strain-dependent MIT. The relative effect of strain in these processes can be expected to be strongly temperature dependent.

Here, we report on experimental studies of the interplay between the MIT and ferroelastic behavior in VO₂ single-crystalline quasi-2D nanoplatelets (NPIs). The NPIs possess most of the unique properties of VO₂ nanobeams and yet have an extensive planar surface, which is required for many applications such as optical modulation, electromechanics, and sensing. “Opening” the second dimension in these quasi-2D NPIs beyond a critical size results in formation of homophase ferroelastic domain structures due to possibility of geometrical frustration. This stems from the fact that a domain structure formed in the low-symmetry phase is such that the symmetry of the parent, high-symmetry phase is preserved on average, as follows from the Curie principle.²³ In 2D systems (with a second dimension larger than the characteristic Kittel domain size), a consequence of this is formation of multiple domain families in the low symmetry phase. Notably, it is possible to control the process of the ferroelastic domain formation through tuning of the strain field mechanically or by NPI–substrate coupling. The goal of this paper is to explore the basic aspects of the homophase and heterophase domain systems in VO₂ single-crystalline NPIs.

VO₂ NPIs and nanowires were grown on SiO₂/Si (Si₃N₄/Si or quartz) substrates using a precursor vapor and argon (13 Torr, 3 sccm flux) as a carrier gas, similar to the protocol used in ref 14. The source material was VO₂ fine powder heated to 1000 °C, and a collecting target (substrate) was placed directly into the source boat. X-ray diffraction (XRD) spectra of samples with different fractions of NPIs on the surface showed that NPIs do not produce any new reflection peaks different from those reported earlier for VO₂ nanobeams implying that in the metallic phase the single-crystalline NPIs are elongated along the tetragonal *c* axis with the upper surface being a (1 10) plane of the tetragonal phase.¹⁴ As verified by optical microscopy and atomic force microscopy (AFM) measurements, the NPI thickness varies from 500 to 700 nm and is uniform along the NPI length. The latter can be as large as few hundred micrometers, while the NPI width is usually below 10 μm. There was no attempt to tune growth parameters in order to gain control over sub-

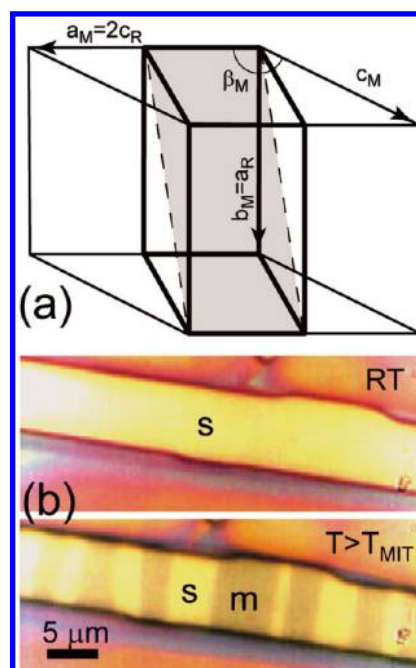


FIGURE 1. (a) Schematic of relationship between tetragonal R and monoclinic M1 unit cells of VO₂. The tetragonal cell is shown with thick lines. Gray is the plane corresponding to the NPI surface. (b) Bright-field optical images of an NPI taken in natural light at room temperature (upper panel) and during the phase transition over the temperature (lower panel). Metallic (R-phase) domains are darker.

strate-imposed strain; however, the latter can be controlled through substrate–NPI coupling and mechanical stress as described and analyzed below.

To study and visualize the nucleation and dynamics of homo- and heterophase domain patterns in VO₂, we employed polarized light microscopy complemented by AFM with simultaneous scanning near-field microwave microscopy imaging.²⁴ Temperature control of a sample during measurements was achieved via Joule heating of the Si substrate by a dc current running through it. A miniature thermocouple attached to the substrate surface was used for temperature measurement. Additionally, room temperature phase composition and structure analysis of the NPIs were performed with general purpose X-ray diffraction (Cu Kα radiation, a Micro Materials Analyzer MMA005 diffractometer from GBC Scientific Equipment Pty Ltd.), polychromatic X-ray microdiffraction (at beamline 34-IDE of Advanced Photon Source at Argonne National Laboratory), and micro-Raman spectroscopy (Renishaw 1000 micro-Raman spectrometer).

At the structural transition in unconstrained bulk samples on cooling, the tetragonal crystal lattice of the compound is discontinuously distorted to monoclinic, so that its tetragonal *c* axis increases by about 1.0% and *a, b* axes decrease by about 0.5% with a small difference between *a* and *b* lattice constants.²⁵ Thus, at the transition temperature, the unit cell volume discontinuously decreases by about 0.044%. This monoclinic structure stable at ambient conditions in pure

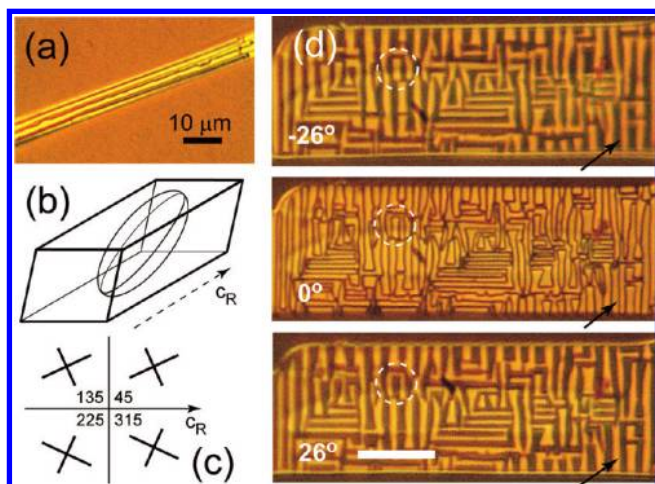


FIGURE 2. Examples of (a) lamellar and (d) labyrinth patterns of ferroelastic domains in NPIs. The images were taken with a polarized light microscope in transmission with crossed polarizer and analyzer. (b) Approximate position of the optical indicatrix with respect to the monoclinic unit cell of the M1 phase. (c) Orientation of the principal axes of the optical indicatrix in the NPI surface for all four possible ferroelastic domain species. Part d demonstrates images corresponding to full extinction in groups of domains. Image at 0° is taken when the polarization direction of one of the polarizers (crossed at 90°) is parallel to the NPI edge. In this position, domain walls are visible, but domain groups are indistinguishable. By turning the sample 26° clockwise and counterclockwise, two different groups of domains become maximally dark (extinct), and the -26° and 26° domain images look like negatives of each other (note a Π -like feature in the white circles and a “6”-like feature denoted with the arrows). This proves that the domains are twins of one and the same structure. Scale bar is $10 \mu\text{m}$.

bulk VO_2 is denoted as M1 phase. Figure 1a depicts the relationship between tetragonal and monoclinic lattices of VO_2 . Here and in the following, we use the coordinate system of the parent phase, as is customarily done in the analysis of the domain structure of ferroic materials. Another metastable semiconducting monoclinic structure—M2 phase—can be stabilized at room temperature by doping,^{26,27} defects,²⁸ or uniaxial stress²⁹ in bulk samples as well as in VO_2 nanobeams by stress due to interaction with a substrate and/or surface tension.^{17,30} Phases M1 and M2 have mutually orthogonal directions of monoclinic shear distortion of the rutile structure, namely, parallel and perpendicular to the tetragonal c_R axis of the parent phase, respectively.

Figure 1b shows bright-field optical images of a few micrometer wide quasi-2D NPI taken in reflection in natural light at two temperatures. As in the case of nanobeams, the metallic phase can be easily identified as higher optical density (darker) stripes as opposed to the lower optical density (brighter) semiconducting phase stripes. At the same time, as illustrated in panels a and b of Figure 2, room temperature polarized light images reveal rich domain patterns, which can be attributed to twinning of the low-temperature phase or to formation of mixed M1/M2 composition. These domains are not seen in natural light. The appearance of domains in the insulating phase is a very general phenomenon in our experiments and does not depend on the

substrate used for growth. Polarized light microscopy reveals very similar domain patterns for all substrates we used, and essentially all NPIs on substrates reveal some domain structures under polarized light at room temperature.

In order to rule out the possibility of M2 phase formation, we have performed direct microstructural analysis with focused ($\sim 0.5 \mu\text{m}$ diameter) polychromatic synchrotron radiation³¹ and with micro-Raman spectroscopy. For micro-beam Laue XRD measurements, the NPIs were grown on $1 \mu\text{m}$ thick Si_3N_4 TEM membranes. We have scanned across individual NPIs with $\sim 0.5 \mu\text{m}$ steps, as well as acquired Raman spectra and Laue patterns randomly from different NPIs. Indexation of over 100 diffraction peaks in each Laue diffraction pattern confirmed the M1 lattice structure. Neither of the techniques showed presence of the M2 phase at room temperature in these NPIs. (See Supporting Information for details of XRD curves, local micro-Laue patterns, and micro-Raman spectra.)

Concluding that the NPIs are entirely in the M1 phase, the formation of the domain structure observed at room temperature can be explained as follow (see, e.g., refs 23, 32, and 33). The monoclinic low-temperature M1 phase of VO_2 has lower symmetry than the high-temperature rutile phase. In such a symmetry-lowering transition, large samples (with long-range strains) are expected to break into orientational domains (twins). A domain structure arises because the system has multiple energy-equivalent orientations to reduce symmetry on cooling through the transition point, and only one way is realized at each point in the sample volume. Generally, domains of different orientations are expected to appear in equal amounts to preserve the symmetry of the high-temperature parent phase in average, especially in a first-order transition proceeding through inhomogeneous activation-driven nucleation of a new phase within a parent phase. Moreover, after the transition is complete, the domains of different types will be approximately equal in size since no type has an advantage from the point of view of energy. However, any external constraints will significantly influence the domain structure in a particular sample because a solid in this case will be forced to keep its shape and volume as close as possible to those in the high-temperature phase. Since domain walls bring additional energy in a system, in the absence of constraints, there is a driving force increasing the domain size. The monoclinic structure of the low-temperature phase possesses biaxial birefringence, and therefore ferroelastic domains in M1 can be readily observed using a polarized light microscope, but not in natural light. The point symmetry group of the tetragonal R phase is $4/mmm$ (space group $P4_2/mmm$) and that of the monoclinic M1 phases is $2/m$ (space group $P2_1/c$). From group-theoretical considerations, there can be four orientations of transformational domains in the low-symmetry phase associated with the structural transition $4/mmm \rightarrow 2/m$.^{34,35} These four domain species can be generated through rotation of the

monoclinic lattice by 90° around the 4-fold axis of the parent phase (around the tetragonal c axis).

We note however that only two kinds of domains are apparently seen in the optical images in panels a and b of Figure 2. In turn, this observation can be explained by the fact that the ferroelastic domain species of the M1 phase are pairwise indistinguishable in the geometry of the optical observation. Indeed, the monoclinic distortion of the tetragonal structure causes rotation of the optical indicatrix by a certain angle around the 2-fold symmetry axis b (common to both R and M1 structures) as schematically illustrated in Figure 2c. The 2-fold axes make an angle very close to 45° with the NPI surface in all possible domains in the studied NPIs. Then the principal axes of the indicatrix in the NPI surface will be oriented as shown in Figure 2d for all four possible directions of the 2-fold axis in the domains. Ferroelastic domains with nonparallel in-surface indicatrix axes will be distinguishable in a polarizing microscope by rotating a sample between crossed polarizer and analyzer, whereas those with parallel axes will not be. This conclusion is supported by measurements of extinction angles for domains by rotating a sample between crossed polarizers. The extinction angle of a domain corresponds to the position at which this domain gets maximally dark. At this angle one of the main axes of the indicatrix in the domain is parallel to the polarizer (or analyzer); the angle is referenced to some easily identified direction of a crystal specimen. A natural reference in our case is a NPI side parallel to the parent phase c axis. In this way a particular domain can be distinguished from others because the optical indicatrix is unambiguously positioned in respect to the crystal lattice of a material. The extinction angle for one of the observed domain groups referenced to the tetragonal c axis was measured to be 26° , in a very good agreement with the value 26.3° obtained from the angle of the oblique extinction of 35° found in ref 36 after recalculation for a cut along a $(\bar{1}10)$ plane. Extinction angles for adjacent domains of M1 phase should be equal but have opposite signs, which is observed in the experiments as is illustrated in Figure 2d. It is worth noting that the extinction angle for the M2 phase would be equal to zero.

In heating-cooling experiments under a polarizing microscope, we observe that during the course of the MIT transition, NPIs are split into both heterophase (metallic/semiconducting) and homophase (ferroelastic) domains, apparently with the domain system configuration attempting to minimize the overall free energy of the system at each stage of the transition. Both heterophase and homophase domains are highly mobile during the transition (see Supporting Information for a video clip showing the domain dynamics during the phase transition).

As seen in panels a and d of Figure 2, pronounced features of the ferroelastic domain structures have a characteristic domain size of about $1\ \mu\text{m}$ and larger, with domain walls predominantly oriented along the $[001]_R$ direction and perpendicular to it (indexing in the parent phase lattice). In

narrower NPIs, the domains tend to form lamellar structures with domain walls oriented along the tetragonal c axis (Figure 2a). In wider NPIs, domains are self-organized into labyrinth structures (Figure 2b). Some NPIs show very large domains (see Supporting Information for corresponding polarized light microscopy images), which probably should be attributed to a more complete strain relaxation. This can be confirmed by the fact that partial chemical etching of the underlying SiO_2 substrate oxide enlarges the size of the ferroelastic domains and complete release of the NPI from the substrate eliminates the domain pattern in most cases (see Supporting Information for illustrating images). The variation of the strain relaxation from NPI to NPI is most probably responsible for the variety of the patterns observed for ferroelastic domains.

To estimate the magnitude of these effects, we assume an average linear expansion coefficient for Si in the temperature range from room temperature to $1000\ ^\circ\text{C}$ to be $4 \times 10^{-6}\ \text{K}^{-1}$.³⁷ The linear expansion coefficient of VO_2 is strongly anisotropic being about five times larger in the c_R direction than perpendicular to it. On the basis of the data of ref 25, we assume its average value in the same temperature range to be $25 \times 10^{-6}\ \text{K}^{-1}$ for the c_R direction and $4.5 \times 10^{-6}\ \text{K}^{-1}$ along the a_R direction. Right before the start of the transition on cooling, the NPIs are under largest tensile stress along their length. Calculation based on the difference in the linear expansion coefficients of VO_2 and silicon yields a strain value of 2.1% in the longitudinal direction. This value is fairly large and should be considered as an upper boundary for the longitudinal strain. We expect that such a large strain should be partially relaxed by slippage at the NPI-substrate interface, differently from NPI to NPI depending on how firmly an NPI is attached to the substrate. This is reflected in the variations of the domain patterns between NPIs and also within each individual NPI observed in the experiments.

Taking into account the change of the lattice parameters due the phase transition ($+1\%$ and -0.5% in the c_R and a_R, b_R directions, respectively), at room temperature, the NPIs should be under tensile strain of $<1.2\%$ along their length and $\sim 0.5\%$ along the width, with almost all the strain across the width arising due to the phase transition. We note that these orthogonal strains have opposite effects on the transition temperature. Whereas tensile stress along the tetragonal c direction raises the MIT temperature, the tensile stress across the NPI width lowers it. This competition apparently broadens the transition, as we observe heterophase coexistence over a temperature range from about 55 to $140\ ^\circ\text{C}$ in some NPIs. In contrast to low-temperature twins, the heterophase domain boundaries are oriented perpendicular to the NPI length with domains spreading across the whole width. On the other hand, the anisotropy of strain together with crystallographic anisotropy results in formation of labyrinth structures of homophase domain patterns in broader NPIs. Similar labyrinth domain patterns appeared in the phase field simulations of polymorphic phase transi-

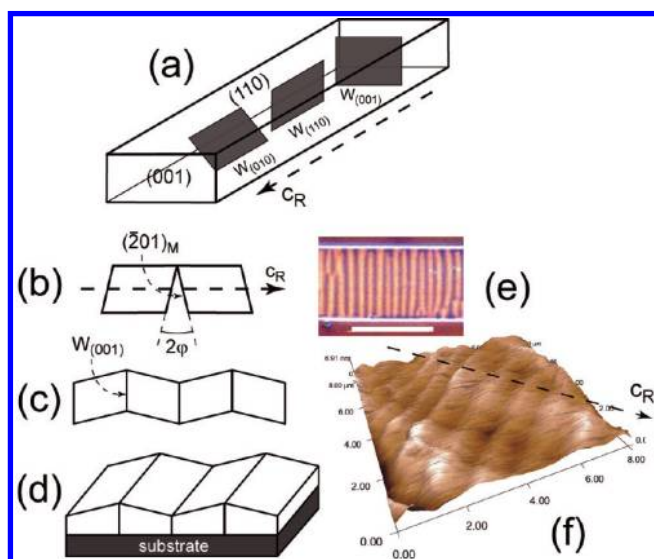


FIGURE 3. (a) Schematic of fixed-type (W_f) ferroelastic domain wall orientations in VO_2 NPIs. (b) Two adjacent monoclinic domains rotated by 180° with respect to each other about the tetragonal axis c_R . In order to keep the mechanical integrity of the structure, domains have to be turned by a clapping angle φ toward each other. (c) A resultant chain of such unconstrained domains. (d) Same domain structure when attached to a substrate. (e) An optical image taken in a polarizing microscope over a parallel-plane 180° domain structure. (f) Topography of NPI surface corresponding to the structure shown in (e). Scale bar in (e) is $10\ \mu\text{m}$.

tions in constrained layers by Artemev et al.³⁸ in the presence of in-plane anisotropy.

To get a more complete understanding of the ferroelastic domain pattern, we turn to the analysis of possible domain walls in the monoclinic phase. As we observe, in a majority of the NPIs, domain walls run perpendicular and along the NPI length. In an unconstrained crystal, the condition of mechanical compatibility between domains allows a crystallographically fixed (W_f type) wall along $\{110\}_R$ planes of the parent phase between 90° domains ($W_{(110)}$ wall) and a fixed wall along $\{010\}_R$ planes between 180° domains ($W_{(010)}$ wall).^{35,39,40} Figure 3a schematically shows the orientations of fixed-type permissible ferroelastic domain walls in the VO_2 NPIs. $W_{(110)}$ walls are oriented along the normal to the NPI surface, parallel (edge-on) to the observation direction in the optical microscope. To keep mechanical integrity of an NPI along a wall, 90° domains should be rotated in this case as rigid bodies by a small angle (so-called twin obliquity or clapping angle^{39,40}) of 0.05° . Apparently, appearance of this wall does not cost much energy to the system. By contrast, a $W_{(010)}$ wall should make an angle of approximately 45° with the NPI surface and be visible in the optical microscope as a $\sim 0.5\ \mu\text{m}$ thick region with brightness gradient. Such walls, however, were not observed in our samples. We speculate that forced alignment of a $W_{(010)}$ wall along the surface normal would be associated with a large lattice stress and energetically unfavorable. Two 180° domains can be separated by a 90° domain instead of a wall with a relatively small energy associated with creation of two

90° walls. This suggests the absence of the 180° domains separated by walls running along NPIs.

There can be two kinds of permissible domain walls with their normals lying approximately along the $[001]_R$ direction of the parent phase in an unconstrained sample: one of the fixed W_f type and one of the so-called S type.^{35,39,40} The former is formed between 180° domains and oriented along the $\{001\}_R$ planes of the parent phase ($W_{(001)}$ wall), i.e., has its normal parallel to the NPI length. We note that because of the monoclinic distortion, the neighboring domains in the 180° domain pairs of this type have to be rotated by a clapping angle φ (Figure 3b,c) in order to keep the mechanical integrity of a NPI. Bearing in mind that the flake surface corresponds to a $\{110\}_R$ plane of the tetragonal lattice, we calculated the value of the clapping angle to be $\varphi = 0.23^\circ$ in this case which implies that a fairly large stress is associated with the walls of this type as is clear from Figure 3d. On the other hand, the orientation of the S -type wall in the lattice depends on the length of the unit cell vectors. This wall separates 90° domains and can be indexed $\{112\}$ in the parent phase meaning an angle of 24° between the wall normal and c_R -axis in an unconstrained structure. Calculations show a clapping angle $\varphi \approx 0$ for this type of walls. S -type walls contain a $\langle 110 \rangle_R$ direction, and therefore their orientation is within a few tenths of degree along the normal to the nanoplatelet surface. We can expect that since the NPIs are under tensile stress along their length, there is a force turning walls of this type across the NPIs length, which makes them indistinguishable from the $W_{(001)}$ walls in an optical microscope. Apparently, walls of this type are present in the NPIs because they are required in order to form the labyrinth domain structures predominantly observed in wider NPIs. All types of domain walls may bend and deviate from their orientations in the unconstrained structure under the action of the local mechanical stresses.

One very distinct homophase domain pattern frequently forms in NPIs. It closely resembles the overwhelmingly observed heterophase domain pattern with domain walls running across a NPI through all of its width. An example of such a situation is shown in Figure 3e. In optical experiments with varying temperature, it was observed that the period of heterophase domain pattern is identical to that of homophase structure in this case. An AFM image of the area (Figure 3f) reveals parallel ridges and valleys on the NPI surface. The period of the topographic features and the period of visible domains in the optical images are the same. Obviously, ridges and valleys on the surface correspond to domain walls and are a result of clapping of neighboring domains. Domain clapping angles can be determined from the AFM image of Figure 3f and were found to be in the range $0.2\text{--}0.3^\circ$, which is in a good agreement with the calculated value of 0.23° for 180° domain walls. We conclude that this pattern consists of 180° domains separated by $W_{(001)}$ walls.

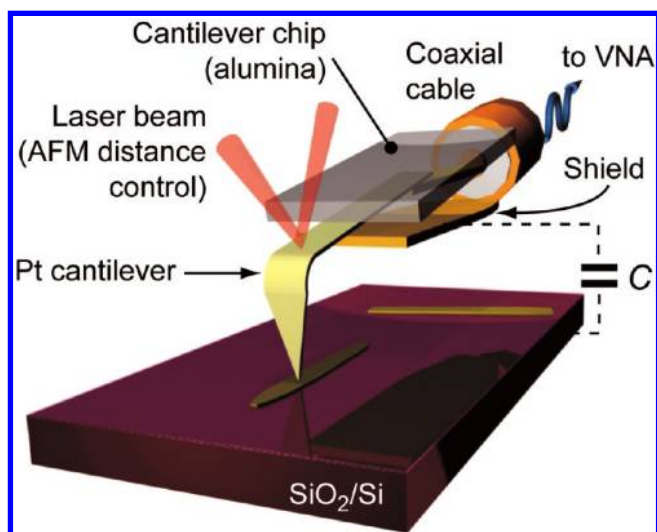


FIGURE 4. Schematic of the SMM probe tip in contact with a sample. The tip cantilever is connected to the central conductor of a coaxial cable. VNA stands for vector network analyzer. C is the capacitance between the conducting substrate and the probe shield.

It is worth noting that analysis of permissible domain walls for phase M2 shows that this phase does not have permissible walls perpendicular to the c axis of the parent phase, and therefore, in the case of R-to-M2 transition, one would have to expect no labyrinth structures, or structures similar to the parallel-plane 180° domain structures found in phase M1. This serves as an additional proof that our NPIs are in the M1 phase at room temperature.

To gain deeper insight into nucleation and growth dynamics of metallic domains, we employed near-field scanning microwave microscopy (SMM) imaging²⁴ of the MIT as a function of temperature. The experimental configuration is shown schematically in Figure 4. A solid wire cantilever tip (Rocky Mountain Nanotechnology) was connected to a coaxial cable (transmission line) through an impedance transformer and then to a vector network analyzer (VNA) (Agilent E5062A). Amplitude and phase of the microwave signal reflected from the tip (S_{11}) were measured while scanning over the sample surface in contact AFM mode. The system is realized on an Asylum Research MFP-3D AFM platform. Microwave microscopy was conducted at a frequency of 1.78 GHz. The advantage of microwave imaging over conducting AFM is that it does not require fabrication of a second electrode over the NPIs because the electrical circuit is complete through displacement currents between the AFM tip, sample, and outer conductor of the microwave line. The microwave signal carries information about conductivity of the materials directly under the tip. The very same tip is used for simultaneous contact AFM topography imaging. We found that deposition of an electrode over an NPI can influence the delicate ferroelastic domain structure in the electrode vicinity and affect the phase transition dynamics. Therefore, it should be avoided. In contrast, SMM provides a noninvasive imaging method. The imaging resolution of this

technique in the present case is determined by the radius of the probe tip and, therefore, is approximately equal to the resolution with respect to topography, i.e., ~ 20 nm in our case. However, the resolution is significantly limited by the sensitivity of the microwave electronics. In the configuration used, the minimal detectable area of a metallic patch imbedded into semiconducting matrix was $\sim 0.12 \mu\text{m}^2$.

The SMM set of images in Figure 5a shows heterophase domain pattern development in a NPI with a labyrinth homophase domain pattern clearly visible in the optical image (Figure 5b) taken with polarized light at room temperature. This pattern does not produce any pronounced topographic features in contrast to the 180° domain structure shown in Figure 3f. Apparently, this is due to a small clapping angle of the 90° domain walls. Each SMM image in Figure 4a corresponds to a certain temperature in the MIT range and was obtained by overlaying a microwave signal over topography. The white color corresponds to the metallic phase while the blue one shows the semiconducting phase. As is seen, the metallic domain formation starts upon cooling with irregularly shaped domains elongated across the NPI. They grow laterally into wider stripes spanning the whole NPI width so that domain boundary normals turn close to the direction parallel the NPI length (see also Figure 5c for optical image of the same area). Due to a larger lattice constant of the metallic phase perpendicular to the tetragonal c axis, there are steps in the NPI thickness at the heterophase domain boundaries. The step height agrees well with that obtained from the data on the lattice constant change and NPI thickness. Upon further heating, metallic domains grow at the cost of the semiconducting phase by the motion of domain walls. Domains may rearrange so that some areas, where transition to the metal phase had already occurred, become again semiconducting, as can be seen from comparison of SMM images taken at 110 and 130 $^\circ\text{C}$. This locally re-entrant phase transition behavior is unusual and clearly illustrates the role of long-range elastic interactions and mobile boundary conditions on the MIT transition dynamics. On the basis of the results, we conclude that AFM–SMM combination with sub-100-nm spatial resolution has a significant potential for providing details of both heterophase and homophase domain structure dynamics during the MIT.

A simple and general phenomenological consideration based on the Ginzburg–Landau approach provides a broader context over the phase transition in NPIs attached to a substrate (clamped) and sheds light on the set of parameters responsible for the observed behavior of the material. (Examples of rigorous analytical treatments of polydomain structures can be found elsewhere, e.g., in ref 41.) We start the general—not restricted to only the VO_2 case—analysis assuming that during the phase transition a clamped and initially strained sample is segregated into domains of the low-temperature phase (I) with an order parameter $\eta \neq 0$ and of the high-temperature phase (M) with $\eta = 0$. If the

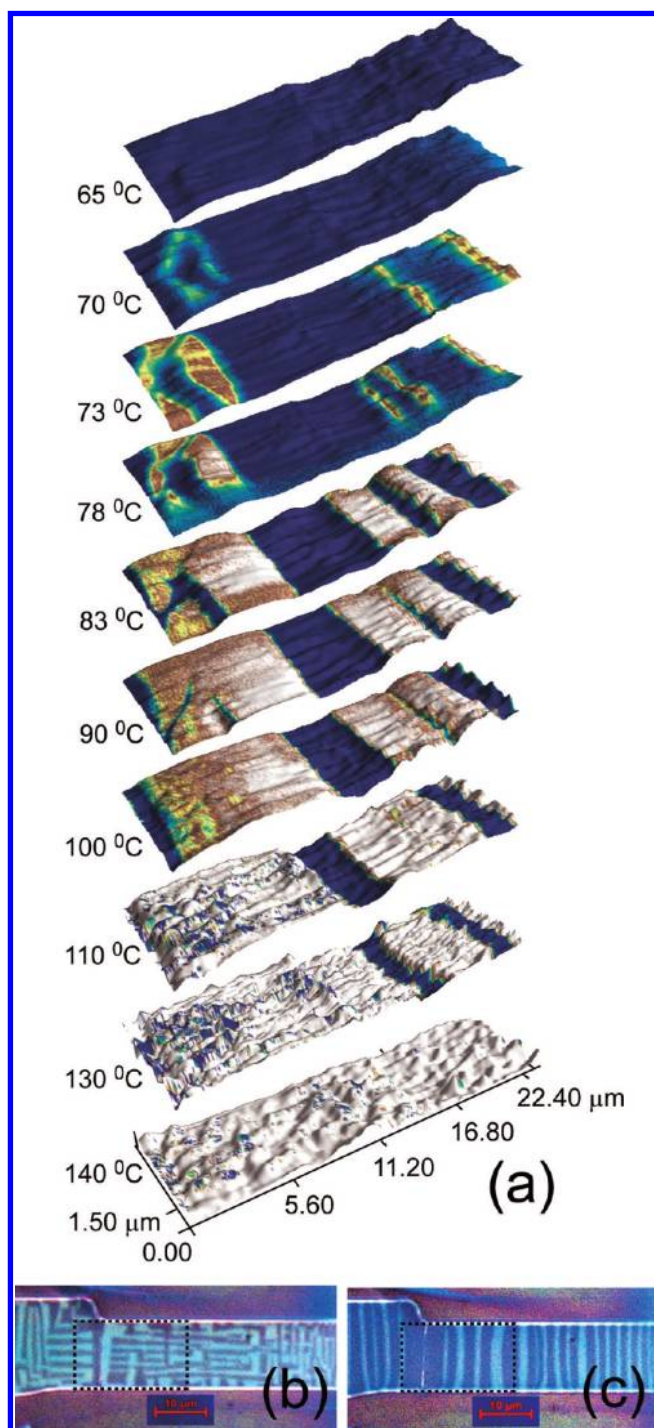


FIGURE 5. (a) Scanning near-field microwave microscopy images of the MIT transition in a VO₂ NPI. The images were taken during heating over the same area at different temperatures indicated near each image. The white color corresponds to high conductivity (metallic phase). Semiconducting phase is blue. (b) and (c) Optical images of the same NPI taken in a polarizing microscope at room temperature and during the MIT, respectively. Dashed line indicates the area used for microwave microscopy shown in (a). Domain structures are not exactly reproducible during thermal cycling. Since optical and SMM images were taken during different cycles, the domain structures in (a) and (c) are somewhat different.

relative population of the I and M phases is x and $(1 - x)$, respectively, the Landau–Devonshire (LD) functional can be presented in the following form

$$F = \left[\Phi(\eta) + \kappa\eta^2 u_I + \frac{K}{2} u_I^2 \right] x + \left[\frac{K}{2} u_M^2 \right] (1 - x) \quad (1)$$

where K is the elastic constant assumed to be same for both phases and κ is the coupling constant of the order parameter with an elastic strain of the sample in the domains of the semiconducting phase u_I (u_M is the elastic strain in the M phase domains).

$$\Phi(\eta) = \frac{1}{2} t \eta^2 + \frac{1}{4} b \eta^4 + \frac{1}{6} d \eta^6 \quad (2)$$

is the bare LD functional with $t = a(T - T_c)$, where T is temperature and T_c is the temperature of the phase transition in the unstrained bulk material. The coefficient b can be either positive or negative (we assume however that $b > 0$, but this is not important), and d is always positive. A well-known result for an unclamped sample is that the LD functional in the case of a finite coupling between the order parameter and the elastic strain can be written down in the form of eq 2 with a renormalized parameter \bar{b}

$$\bar{b} = b \left(1 - \frac{2\kappa^2}{bK} \right) = b(1 - \lambda)$$

We introduced here a coupling parameter

$$\lambda = \frac{2\kappa^2}{bK} \quad (3)$$

Depending on the sign of \bar{b} , two cases are possible for a strained unclamped sample: (a) if $\bar{b} > 0$ (i.e., $\lambda < 1$), the transition is second order with the critical temperature $t_c = 0$; (b) if $\bar{b} < 0$ (i.e., $\lambda > 1$), the transition is of the first order with superheating/thermodynamic/supercooling critical temperatures given by

$$t_{c+} = 4t_0(1 - \lambda)^2, \quad t_{c0} = \frac{3}{16}t_0(1 - \lambda)^2, \quad t_{c-} = 0 \quad (4)$$

respectively, where $t_0 = b^2/d$.

Considering x , η , u_I and u_M in eq 1 as variational parameters, we take into account the clamping condition for a thin sample attached to a substrate

$$xu_1 + (1 - x)u_M = u_0 \quad (5)$$

where u_0 is a strain in the sample above the transition, in the pure M phase. We exclude u_M and minimize F over u_1 and x . The calculation yields the following:

(1) The temperature scale is renormalized as $t' = t + \kappa u_0$, which means an increase of the critical temperature due to the tensile stress due to a substrate.

(2) A mixed I/M state exists between critical temperatures t'_{c1} and t'_{c2} ($t'_{c2} > t'_{c1}$; $x(t'_{c2}) = 0$, $x(t'_{c1}) = 1$) defined by

$$t'_{c2} = \frac{3}{16}t_0(1 - \lambda)^2, \quad t'_{c1} = \frac{3}{16}t_0(1 - \lambda)(1 + 3\lambda) \quad (6)$$

The splitting of t'_c into t'_{c1} and t'_{c2} occurs at $\lambda > 1$, when transition in an unclamped sample becomes of the first order. The corresponding phase diagrams are shown in Figure 6.

(3) The I phase population parameter x gradually changes with temperature (no first order jumps) between t'_{c1} and t'_{c2}

$$x(t') = -\frac{4}{3} \frac{t'_{c2} - t'}{t_0 \lambda (1 - \lambda)} \quad (7)$$

All these results for $\lambda > 1$ qualitatively agree with the experimental observations. Especially, we note that the phase transition range in Figure 5a spans from about 65 to 140 °C suggesting that the critical temperature of the MIT is increased from $T_c = 68$ °C of the unstrained bulk materials because of a tensile stress in NPLs at the phase transition temperature due to differences in the linear expansion of VO₂ and substrate as discussed above.

Finally, we were able to manipulate the homophase domain structures through an external mechanical stress. Figure 7, made in polarized light, depicts a variation of the ferroelastic domain pattern in a quasi-2D NPL as a function of NPL bending. The right half of the NPL is strongly bound to the substrate while the left one is released. Mechanical bending induced by the tip of a micromanipulator causes reorganization of the domain structure in response to the stress application. Similar to the strain engineering approach to control the organization of heterophase domains in nanobeams reported in ref 19, we demonstrate that the same can be performed with homophase domains in quasi-2D NPLs. This opens up exciting opportunities to actively control optical and electrical properties of NPL by means of elastomechanical actions.

To summarize, development of the lateral dimension in quasi-2D NPLs of VO₂ results in formation of a variety of ferroelastic homophase domain structures in the low symmetry monoclinic M1 phase after completion of the MIT transition on cooling. The ferroelastic domain structure of

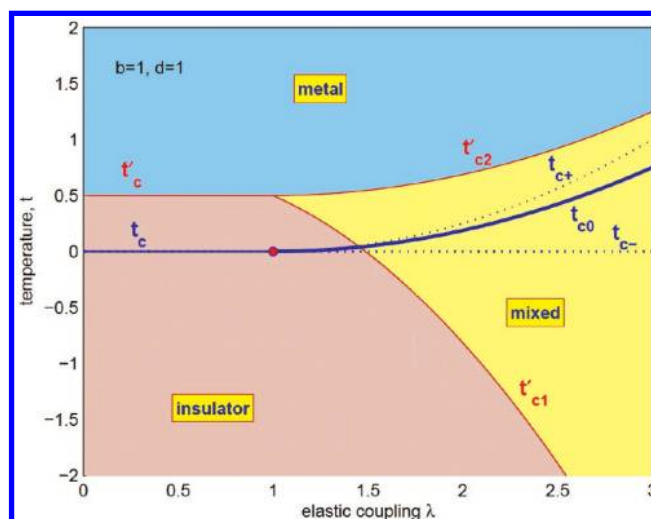


FIGURE 6. Phase diagram of the metal–insulator transition in a clamped sample as a function of the order parameter–strain coupling constant, λ . The mixed M/I domain state exists between critical temperatures t'_{c1} and t'_{c2} when $\lambda > 1$. For comparison, we present the phase diagram of a free-standing bulk sample, in which coupling with elasticity results in renormalization of the transition to the first-order transition at $\lambda > 1$ (blue lines). t_{c+} and t_{c-} correspond to superheating and supercooling temperatures, respectively. Transition in the sample is shifted to higher temperatures due to a tensile stress.

the low-temperature semiconducting phase is dependent on the NPL lateral size and nanoplatelet–substrate interaction, with lamellar patterns being characteristic for narrower nanoplatelets and labyrinth patterns for wider ones. Weaker NPL–substrate interaction leads to larger and less regular domain patterns. On the basis of group-theoretical considerations, we have identified ferroelastic domain species and domain walls. A periodic structure of metal and semiconducting domains arising during the phase transition frequently evolves into a structure consisting of alternating ferroelastic domains being mirror images of each other and separated by domain walls perpendicular to the tetragonal c axis of the metallic phase. By applying AFM for topographic imaging with simultaneous near-field microwave microscopy and optical imaging, we were able to follow details of the heterophase structure development and associated changes in NPL surface topography, starting from metallic domain nucleation. These insights into domain nucleation and dynamics and underlying mechanisms of domain pattern formation are of significant importance for a large spectrum of potential applications of this form of VO₂.

Acknowledgment. The authors thank Alexander Tagantsev (EPFL, Switzerland) for fruitful discussions and Wenjun Liu for help in obtaining X-ray microdiffraction measurements at the APS. Research at Oak Ridge National Laboratory’s Center for Nanophase Materials Sciences was sponsored by the Scientific User Facilities Division, Office of Basic Energy Sciences, U.S. Department of Energy. The research at SIUC was supported through NSF ECCS-0925837 and SISGR-DOE ERKCM67. The work of I.L. was supported by ANR project

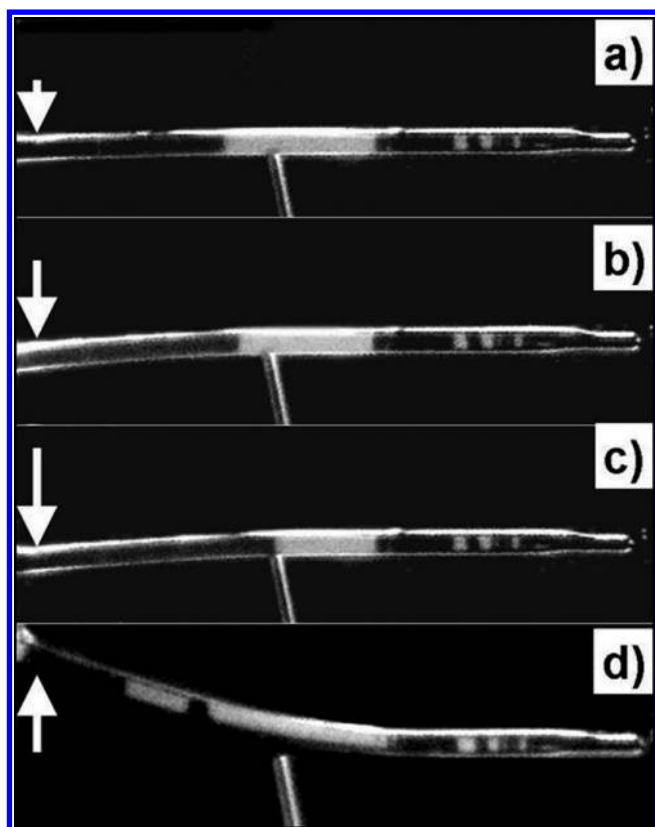


FIGURE 7. Manipulation of a ferroelastic domain pattern with mechanical stress. The image was taken in polarized light at room temperature. The right half of the VO₂ NPI is fixed by a strong interaction with the substrate. The left part of the NPI is detached from the support and can be bent by a micromanipulator probe. Bending of the left part of the NPI leads to movement of domain walls between pairs of homophase domains. The substrate background was digitally removed for clarity.

LOMACOQU, J.D.B. and J.Z.T. were supported by the Division of Materials Sciences and Engineering, Office of Basic Energy Sciences, U.S. DOE. Use of the APS beamline 34-IDE was supported by the Scientific User Facilities Division of BES, U.S. DOE.

Supporting Information Available. Additional images of ferroelastic domain patterns observed in a polarizing microscope in VO₂ NPIs at room temperature, monochromatic X-ray diffraction curves, typical room temperature micro-Raman spectrum of a VO₂ NPI with phase assignment, images illustrating result of partial chemical etching of the SiO₂ support layer on the appearance of ferroelastic domain structure in VO₂ NPIs, a polychromatic X-ray microdiffraction Laue pattern from a nanoplatelet, local pole figures, and a video clip showing dynamics of homophase and heterophase domains during the MIT upon cooling. This material is free of charge via the Internet at <http://pubs.acs.org>.

REFERENCES AND NOTES

- (1) Fan, J. C. C.; Fetterman, H. R.; Bachner, F. J.; Zavracky, P. M.; Parker, C. D. *Appl. Phys. Lett.* **1977**, *31*, 11.
- (2) Jin, P.; Tanemura, S. *Jpn. J. Appl. Phys., Part I* **1994**, *33*, 1478.
- (3) Stefanovich, G.; Pergament, A.; Stefanovich, D. J. *Phys.: Condens. Matter* **2000**, *12*, 8837.

- (4) Kim, H. T.; Chae, B. G.; Youn, D. H.; Kim, G.; Kang, K. Y.; Lee, S. J.; Kim, K.; Lim, Y. S. *Appl. Phys. Lett.* **2005**, *86*.
- (5) Lysenko, S.; Vikhnin, V.; Fernandez, F.; Rua, A.; Liu, H. *Phys. Rev. B* **2007**, *75*.
- (6) Hilton, D. J.; Prasankumar, R. P.; Fourmaux, S.; Cavalleri, A.; Brassard, D.; El Khakani, M. A.; Kieffer, J. C.; Taylor, A. J.; Averitt, R. D. *Phys. Rev. Lett.* **2007**, *99*.
- (7) Muraoka, Y.; Hiroi, Z. *Appl. Phys. Lett.* **2002**, *80*, 583.
- (8) Driscoll, T.; Kim, H.-T.; Chae, B.-G.; Kim, B.-J.; Lee, Y.-W.; Jokerst, N. M.; Palit, S.; Smith, D. R.; Di Ventra, M.; Basov, D. N. *Science* **2009**, *325*, 1518.
- (9) Petit, C.; Frigerio, J. M.; Goldmann, M. J. *Phys.: Condens. Matter* **1999**, *11*, 3259.
- (10) de Almeida, L. A. L.; Deep, G. S.; Lima, A. M. N.; Neff, H. *Appl. Phys. Lett.* **2000**, *77*, 4365.
- (11) Rozen, J.; Lopez, R.; Haglund, R. F.; Feldman, L. C. *Appl. Phys. Lett.* **2006**, *88*.
- (12) Qazilbash, M. M.; Brehm, M.; Chae, B. G.; Ho, P. C.; Andreev, G. O.; Kim, B. J.; Yun, S. J.; Balatsky, A. V.; Maple, M. B.; Keilmann, F.; Kim, H. T.; Basov, D. N. *Science* **2007**, *318*, 1750.
- (13) Baik, J. M.; Kim, M. H.; Larson, C.; Wodtke, A. M.; Moskovits, M. J. *Phys. Chem. C* **2008**, *112*, 13328.
- (14) Guiton, B. S.; Gu, Q.; Prieto, A. L.; Gudiksen, M. S.; Park, H. J. *Am. Chem. Soc.* **2005**, *127*, 498.
- (15) Wu, J.; Gu, Q.; Guiton, B. S.; de Leon, N. P.; Ouyang, L.; Park, H. *Nano Lett.* **2006**, *6*, 2313.
- (16) Strelcov, E.; Lilach, Y.; Kolmakov, A. *Nano Lett.* **2009**, *9*, 2322.
- (17) Sohn, J. I.; Joo, H. J.; Ahn, D.; Lee, H. H.; Porter, A. E.; Kim, K.; Kang, D. J.; Welland, M. E. *Nano Lett.* **2009**, *9*, 3392.
- (18) Wei, J.; Wang, Z.; Chen, W.; Cobden, D. H. *Nat. Nanotechnol.* **2009**, *4*, 420.
- (19) Cao, J.; Ertekin, E.; Srinivasan, V.; Fan, W.; Huang, S.; Zheng, H.; Yim, J. W. L.; Khanal, D. R.; Ogletree, D. F.; Grossman, J. C.; Wu, J. *Nat. Nanotechnol.* **2009**, *4*, 732.
- (20) Morin, F. J. *Phys. Rev. Lett.* **1959**, *3*, 34.
- (21) Chudnovskiy, F.; Luryi, S.; Spivak, B. In *Future Trends in Microelectronics: The Nano Millennium*; Luryi, S., Xu, J. M., Zaslavsky, A., Eds.; Wiley-Interscience: Hoboken, NJ, 2002; pp 148–155.
- (22) Kim, H.-T.; Chae, B.-G.; Youn, D.-H.; Maeng, S.-L.; Kim, G.; Kang, K.-Y.; Lim, Y.-S. *New J. Phys.* **2004**, *6*, 52.
- (23) Salje, E. K. H. *Phase transitions in ferroelastic and co-elastic crystals: an introduction for mineralogists, material scientists, and physicists*; Cambridge University Press: Cambridge (England) and New York, 1990.
- (24) Anlage, S. M.; Talanov, V. V.; Schwartz, A. R., Principles of Near-Field Microwave Microscopy. In *Scanning Probe Microscopy: Electrical and Electromechanical Phenomena at the Nanoscale*; Kalinin, S., Gruverman, A., Eds.; Springer Scientific: New York, 2007; pp 215–253.
- (25) Kucharczyk, D.; Niklewski, T. J. *Appl. Crystallogr.* **1979**, *12*, 370.
- (26) Marezio, M.; McWhan, D. B.; Remeika, J. P.; Dernier, P. D. *Phys. Rev. B* **1972**, *5*, 2541.
- (27) Ghedira, M.; Vincent, H.; Marezio, M.; Launay, J. C. *J. Solid State Chem.* **1977**, *22*, 423.
- (28) Chamberland, B. L. *J. Solid State Chem.* **1973**, *7*, 377.
- (29) Pouget, J. P.; Launois, H.; D'Haenens, J. P.; Merenda, P.; Rice, T. M. *Phys. Rev. Lett.* **1975**, *35*, 873.
- (30) Zhang, S.; Chou, J. Y.; Lauhon, L. J. *Nano Lett.* **2009**, *9*, 4527.
- (31) Ice, G. E.; Pang, J. W. L.; Larson, B. C.; Budai, J. D.; Tischler, J. Z.; Choi, J.-Y.; Liu, W.; Liu, C.; Assoufid, L.; Shu, D.; Khounsary, A. *Mater. Sci. Eng., A* **2009**, *524*, 3.
- (32) Wadhawan, V. K. *Introduction to ferroic materials*; Gordon & Breach: Amsterdam, 2000.
- (33) Tagantsev, A. K.; Fousek, J.; Cross, L. E. *Domains in Ferroic Crystals and Thin Films*; Springer: New York, 2010.
- (34) Aizu, K. *Phys. Rev. B* **1970**, *2*, 754.
- (35) Erhart, J. *Phase Transitions* **2004**, *77*, 989.
- (36) Fillingham, P. J. *J. Appl. Phys.* **1967**, *38*, 4823.
- (37) Okada, Y.; Tokumaru, Y. *J. Appl. Phys.* **1984**, *56*, 314.
- (38) Artemev, A.; Slutsker, J.; Roytburd, A. L. *Acta Mater.* **2005**, *53*, 3425.
- (39) Fousek, J.; Janovec, V. *J. Appl. Phys.* **1969**, *40*, 135.
- (40) Sapriel, J. *Phys. Rev. B* **1975**, *12*, 5128.
- (41) Roytburd, A. L. *J. Appl. Phys.* **1998**, *83*, 228.